Electrochimica Acta 462 (2023) 142696

Contents lists available at ScienceDirect

Electrochimica Acta

journal homepage: www.journals.elsevier.com/electrochimica-acta

Graphene vs. carbon black supports for Pt nanoparticles: Towards next-generation cathodes for advanced alkaline electrolyzers

Marilena Isabella Zappia [a,1], Valentina Mastronardi [b,1], Sebastiano Bellani [a,*], Yong Zuo [c], Gabriele Bianca [d], Luca Gabatel [a,e], Matteo Gentile [f], Ahmad Bagheri [d], Hossein Beydaghi [a], Filippo Drago [c], Michele Ferri [c], Mauro Moglianetti [b], Pier Paolo Pompa [b], Liberato Manna [c], Francesco Bonaccorso [a,*]

[a] BeDimensional S.p.A., Via Lungotorrente Secca 30R, Genova 16163, Italy
[b] Istituto Italiano di Tecnologia, Nanobiointeractions & Nanodiagnostics, Via Morego 30, Genova 16163, Italy
[c] Nanochemistry Department, Istituto Italiano di Tecnologia, Via Morego 30, Genova 16163, Italy
[d] Graphene Labs, Istituto Italiano di Tecnologia, Via Morego 30, Genova 16163, Italy
[e] Department of Mechanical Engineering-DIME, University of Genoa, Genova 16145, Italy
[f] Politecnico di Milano, Piazza Leonardo Da Vinci 32, Milano 20133, Italy

ARTICLE INFO

Keywords:
Graphene
Carbon black
Platinum
Electrocatalysis
Cathode
Alkaline electrolyzer
Durability

ABSTRACT

The development of efficient and cost-effective water splitting electrolyzers is a fundamental step to support the achievement of climate neutrality by using renewable energy sources to produce green H_2 as a form of clean fuel. In this work, we investigated Pt-based nanostructured cathodes for high-performance alkaline electrolyzers (AELs), showing the beneficial effect of graphene over traditional carbon black as nanocatalysts support. By relying on a water-based, scalable, synthetic method, surface-cleaned Pt nanoparticles were successfully produced and strongly anchored to defect-free graphene flakes, the latter produced through wet-jet milling exfoliation of natural graphite. Once deposited on conventional gas diffusion layers, Pt/graphene catalysts outperform traditional Pt on Vulcan (Pt/C) in terms of hydrogen evolution reaction (HER) activity and performance durability. The two-dimensional morphology of graphene flakes strongly retains the catalysts in the electrode even in the absence of any binder, while intrinsically ensuring the exposure of the catalytic sites for the HER. This rationale enables the fabrication of high-performance AELs based on Pt/graphene cathodes. By using commercially available cost-effective anodes (stainless-steel meshes), our AELs reached current densities of 1 A cm^{-2} at a voltage of as low as 1.71 V. These AELs can even operate up to more than 2 A cm^{-2} (*e.g.*, 2.2 A cm^{-2} at 1.90 V), with stable performance during accelerated stress tests. Our study discloses two main aspects: (1) graphene is an effective conductive support for 1–10 nm-scale catalysts for the development of nanostructured cathodes with elevated catalytic properties and durable performance; (2) the use of efficient nanostructured cathodes can boost the AEL's performance to state-of-the-art values reported for proton-exchange membrane electrolyzers, avoiding the use of expensive anodes (*e.g.*, Ir-based ones).

1. Introduction

Green H_2 production through water electrolysis powered by renewable energy sources and electricity is in the spotlight to cut greenhouse emissions and reach climate neutrality [1]. Thus, the growth of renewable energy assets operating in both grid-based and decentralized energy solutions must be accompanied by the rapid development of novel water electrolysis plants, enabling efficient storage of renewable electrical energy in form of hydrogen [2]. In this scenario, alkaline electrolyzers (AELs) represent a cost-effective and robust technology for green hydrogen production, and systems with a hydrogen production capacity of hundreds of $Nm^3\ h^{-1}$ are already commercially available [3,4]. Alternative technologies, like proton-/anion-exchange membrane electrolyzers (PEM-/AEM-ELs) and solid-oxide electrolyzers, are currently

* Corresponding authors.
E-mail addresses: s.bellani@bedimensional.it (S. Bellani), f.bonaccorso@bedimensional.it (F. Bonaccorso).
[1] These authors contributed equally to this work.

https://doi.org/10.1016/j.electacta.2023.142696
Received 27 November 2022; Received in revised form 26 April 2023; Accepted 3 June 2023
Available online 4 June 2023

competing with AELs, aiming at minimizing H_2 production costs while increasing production rates. Indeed, traditional AELs operate with reasonable energy efficiency only at low current densities (*e.g.*, $\leq$ 400 mA cm^{-2}), limiting production rates or increasing the complexity and cost of balance of plant compared to PEM-ELs [4,5]. However, recent advances in alkaline electrolysis have changed this commonly asserted scenario, and the AEL technology proved to be as efficient as the PEM- and AEM-ELs even at high current densities (on the order of 1 A cm^{-2}) when state-of-the art diaphragms and electrodes are used [3,6,7].

While Pt-group metal (PGM)-based catalysts are mandatory to withstand corrosion in acidic environments of PEM-ELs [8], their use in AELs is less common, since Earth-abundant metals (*e.g.*, Ni, Mo, Co) and mixed metal oxides are established catalysts for alkaline water electrolysis [9]. Nevertheless, PGMs have been widely used to realize state-of-the-art AELs and AEM-ELs [10–16], and industrial Pt-based AELs have been recently deployed as low-operating expense (OPEX) industrial prototypes, lowering hydrogen cost outlook [17]. Contrary to PEM- and AEM-ELs, which desirably operate with dried cathodes to facilitate H_2 removal [18,19], the electrolyte is continuously supplied to both AEL electrodes, which, in principles, do not require the use of an ion-conducting binder to guarantee ion mobility from the catalytic sites towards the electrode separator. On the one hand, the presence of a binder can electrically insulate the catalytic sites of the catalyst layer, decreasing the AEL performance. [20] Beyond a certain content threshold, Nafion can also impede efficient H_2 gas removal as a consequence of the decrease of the electrode porosity [21,22]. On the other hand, an insufficient binder content may result in poor mechanical properties of the electrodes, and catalyst layer delamination/dissolution can progressively occur in the presence of mechanical stresses induced by cell torque, electrolyte circulation and pronounced gas bubbling [23].

In this work, we prove that graphene can act as advanced carbonaceous support for Pt nanoparticles (NPs) acting as catalysts for the alkaline hydrogen evolution reaction (HER). We show that, while offering most of the advantages of common carbon black supports (*e.g.*, Vulcan XC 72R), including excellent electrical conductivity and processability (easiness to disperse), graphene intrinsically features a two-dimensional (2D) nanocatalyst-anchoring morphology. More in detail, the interaction between sp^2 carbon and surface-cleaned Pt NPs, as well as the large (μm scale) lateral size of graphene flakes, impede the detachment of the catalysts from the electrode through the gas diffusion layer (GDL) during the high-current density operation targeted by practical electrolyzers. Thus, our AEL, implementing a Pt on graphene (Pt/graphene) cathode (and using cost-effective stainless-steel based anodes), reaches current densities of 1 A cm^{-2} at 1.71 V cell voltage, and can even operate up to more than 2 A cm^{-2} (*e.g.*, 2.2 A cm^{-2} at 1.90 V), overcoming state-of-the-art performance for the AELs, to the best of our knowledge [4]. Thus, the well-known barrier properties of graphene [24,25] are herein revisited for the formulation of advanced Pt-based catalysts, which outperform benchmark Pt on Vulcan (Pt/C). The origin of the high performance of our AEL may be also associated to the high catalytic activity recently observed for nanostructured Pt-based catalysts in high-pH media (*e.g.*, 30 wt% KOH) [26], such as those conventionally used for AELs (but not in AEM-ELs [27]). Indeed, massive hydronium ions can be locally generated on the Pt surface during water dissociation and hydrogen adsorption steps [26], leading to an acid-like local reaction environment [26]. Prospectively, graphene-based supports may be considered for advanced catalysts (metal alloys and hybrid catalysts) having a catalytic activity towards the HER superior to that of Pt [28], thus, aiming at realizing AEL with performances surpassing those of PEM-ELs with low PGM-mass loadings [29]. Importantly, other efficient (doped) graphene-supported PGM-based catalysts (*e.g.*, PGM-transition metal alloys and metal single atoms) for the HER in acidic media have been reported in recent literature [30–34], showing performance superior to that of Pt/C benchmark. In this context, our work spurs the validation of such kind of graphene-based catalysts also in alkaline media for their final application in industrial AELs, once their massive production can be met with affordable costs. Notably, efficient AELs with low content of PGMs in their cathodes intrinsically avoid the need of expensive anodes, like those based on Ir (whose global mine production is currently insufficient to meet the demand for tens of GW-scale electrolyzer markets [35]), which are instead required by PEM-ELs to withstand acid-induced corrosion phenomena [36].

2. Experimental

2.1. Materials and reagents

90 × 90 mesh 316 stainless-steel meshes (SSMs), 10 wt% Nafion dispersion (D1021 Nafion™), carbon papers (CPRs) (AvCarb MGL280, 280 μm), and hydrophilic carbon cloth (ELAT, 406 μm) were supplied by Fuel Cell Store. Zirfon Perl UTP 220 diaphragm were purchased from Agfa. Pt/C (C20-PT, 20 wt%) was purchased from QUINTECH. Hexachloroplatinic acid hexahydrate $H_2(PtCl_6)\cdot 6H_2O$ (BioXtra specification), sodium citrate tribasic dihydrate (BioUltra specification), sodium borohydride ($NaBH_4$), and citric acid anhydrous, ethanol (EtOH) (absolute for analysis EMSURE® ACS,ISO,Reag. pH Eur), 2-propanol (IPA) (ACS reagent, ≥99.5%), NaOH (ACS reagent, ≥97.0%, pellets) and KOH (reagent grade, 90% flakes) were purchased from Sigma Aldrich.

2.2. Graphene production

Graphene was produced at BeDimensional S.p.A.'s industrial plant through wet-jet milling (WJM) exfoliation of graphite [37,38] as detailed in patent Nr. WO2017/089987A1 and referring to protocols reported in previous reports [39–42]. Additional details on the WJM exfoliation process are available in the Supporting Information.

2.3. Spherical 5 nm Pt NP synthesis

Spherical Pt NPs (~5 nm diameter) were produced in an aqueous environment without the use of catalysts-poisoning reagents and/or organic coatings, according to the synthesis method described in previous studies [43,44]. Such a synthesis process stabilizes the Pt NPs by citrate molecules [43–45], which can be completely removed by a simple and rapid step in alkaline conditions to obtain coating-free Pt NPs that directly anchor themselves to the carbonaceous supports [43,46]. The synthesis of Pt NPs is fully described in the Supporting Information.

2.4. Material characterization

Bright-field transmission electron microscopy (BF-TEM) images of the graphene flakes and Pt NPs on graphene were acquired using a JEOL JEM-1011 microscope with a thermionic source (W filament) and operated at 100 kV. The samples were prepared by drop casting nanoflakes dispersions onto ultrathin C-film on holey carbon 400 mesh Cu grids (Ted Pella Inc), subsequently washed with deionized water and dried at room temperature in vacuum overnight. Atomic force microscopy (AFM) measurements were acquired with a Dimension Icon atomic force microscope (Bruker). The measurements were carried out in intermittent contact mode using RTESPA cantilevers (Bruker) with a tip with a nominal diameter of 8 nm. A drive frequency of ~300 kHz and a scan rate of 0.7 Hz was used for the image acquisition. The height profile analysis was performed using Gwyddion 2.54 software. The AFM data were analyzed using OriginPro 9.1 software. The samples were fabricated by depositing the nanoflake dispersions onto mica substrates (G250–1, Agar Scientific Ltd.). The samples were dried under vacuum overnight before measurements. Raman spectroscopy measurements were performed using a Renishaw microRaman Invia 1000 spectrometer and a laser wavelength of 532 nm. The as-prepared dispersions were drop-cast onto Si/SiO_2 substrates and dried under vacuum overnight.

The zeta (ζ) potential was measured with a Malvern Instruments Zeta Sizer Nano ZS system (Malvern, U.K.). The measurements for ζ potential of graphene were performed in a mixture of water and EtOH at 25 °C. The measurements for ζ potential of Pt NPs were performed in water at 25 °C before and during the removal of citrate using a basic solution for the Pt NPs.

2.5. Electrode fabrication

The WJM-produced graphene was dried in the form of powder using a freeze dryer [47]. Afterwards, graphene powder was redispersed in a water:EtOH (80:20 vol/vol) mixture at a concentration of 10 g L^{-1}. The so-produced graphene dispersion was diluted by adding Milli-Q water, adjusting the concentration to 1 g L^{-1}. The diluted dispersion was mechanically stirred for 10 min. Then, 5 nm spherical Pt NPs were added with a loading of 20 wt% relatively to the solid content (graphene plus Pt NPs), and the dispersion was sonicated for 10 min. After the adsorption of Pt NPs on graphene, pellets of NaOH were added to the dispersion with a concentration of (20 g L^{-1}) to remove the citrate coating of the Pt NPs, which then anchored themselves to the graphene surface. Then, the excess solvent was removed to obtain a final Pt/graphene water dispersion at a concentration of 200 g L^{-1}. The Pt/graphene electrodes were prepared through spray coating of diluted Pt/graphene dispersion (1 g L^{-1}). A benchmark Pt/C electrode was produced through an identical procedure, but using a Pt/C water:IPA (75:25 vol/vol) ink instead of the diluted Pt/graphene dispersion. The inks were sonicated in an Ultrasonic Bath USC - THD (WVR) for 1 h to be homogeneously mixed. The so-produced inks were hand sprayed on CPRs mounted on a hot plate heated at 140 °C, and the catalyst mass loading (m_{Pt}) (~300 μg_{Pt} cm^{-2}) was controlled by adjusting the amount of the sprayed inks. Rotating disk electrodes (RDE) for the hydrogen underpotential deposition (H_{UPD}) measurements were produced by depositing 20 μL of a Pt/graphene (or Pt/C) dispersion, prepared by adding 1 μL of D1021 Nafion™ Dispersion (10 wt%) to 1 mL of a 1.3 mg mL^{-1} Pt/graphene (or Pt/C) dispersion, onto an RDE with a 5 mm diameter (Pt mass -$mass_{Pt}$- ~5.3 μg), which was dried at 60 °C in the air for 20 min.

2.6. Electrode characterization

The m_{Pt} of the investigated electrodes was measured by inductively coupled plasma optical emission spectroscopy (ICP-OES) using a ThermoFisher iCAP 7600 DUO Thermo spectrometer. The samples were prepared by digesting a piece (0.57 cm^2 area) of the catalyst electrode in HCl/HNO_3 (3:1, vol/vol) for 18 h. The resulting solution was then diluted to 100 mL with Milli-Q water. The ICP-OES measurements were affected by a systematic error of ca. 5%. Experimental m_{Pt} values, measured on different pieces of the produced electrodes, were found to be 296 ± 28 μg cm^{-2} for Pt/graphene and 305 ± 32 μg cm^{-2} for Pt/C. Scanning electron microscopy (SEM) measurements were acquired on a JEOL JSM-6490LA microscope operated at an acceleration voltage of 5–10 kV, while energy-dispersive X-ray spectroscopy (EDS) measurements were performed at 20 kV. To acquire reliable Pt:C weight ratios, rather than specific values from a very small spots, EDS maps were recorded from large areas where the CPR fibers were well-covered by the Pt/graphene catalytic layer to exclude the contribution of C element from the GDL. The obtained Pt and C atomic contents were used for the calculation of Pt:C weight ratio, confirming the values expected from the EDS analysis of the Pt/graphene powders. A potentiostat/galvanostat (VMP3, Biologic) equipped with an external high-current booster channel was used to perform the electrochemical measurements of the electrodes at room temperature, using a three-electrode cell configuration in a polytetrafluoroethylene (PTFE) cell. A Pt wire was used as the counter electrode. A 6 M KOH-filled Hg/HgO electrode with a PTFE-body was used as the reference electrode for alkaline media. The reference electrode was calibrated using standard calibration protocols [48]. The electrolyte was 1 M KOH. The Pt electrochemically active surface area (ECSA) of Pt/graphene (or Pt/C) catalysts was measured through the H_{UPD} methods [49,50] performing cyclic voltammetry (CV) measurements on RDE at 50 mV s^{-1} potential scan rate. The 50th CV curve was analysed for the ECSA calculation. The ECSA was determined by charge integration of the hydrogen adsorption region (Q_H-upd) after performing a double-layer current correction. Considering a theoretical charge of 210 μC cm^{-2} for the adsorption of a monolayer of hydrogen at the surface of polycrystalline Pt (Q_{mono}) [50] $mass_{Pt}$-normalized ECSA was calculated as:

$$Q_{H-upd}/(Q_{mono} \times mass_{Pt})$$

A multistep chronopotentiometry (CP) protocol was used to acquire the galvanostatic polarization curves of the electrodes. The cathode potential was measured over 5 min for each current step. The potentials at the end of each current step were used to provide the points of the polarization curve. The galvanostatic polarization curves were iR-corrected (i is the measured working electrode current and R is the series resistance) considering R as the high-frequency resistance measured through electrochemical impedance spectroscopy (EIS) measurements of the electrodes. The series resistance was measured for each current step to consider possible resistance during measurements. Indeed, resistance change may be caused by gas bubbles formation and temperature variation [51]. Potentiodynamic linear scan voltammetry (LSV) measurements were also conducted using a 2 mV s^{-1} potential scan rate. The potentiodynamic LSV curves were iR-corrected by measuring R at the open circuit potential.

2.7. Alkaline electrolyzers assembly

The 1 cm^2-AELs were produced by modifying a commercially available zero-gap single electrolysis cell hardware (Dioxide Materials), including corrosion resistant Ni-based anode and cathode flow field (bipolar) plates, O-ring seals, and PTFE gasketing. Zirfon Perl UTP 220 was used as the diaphragm. A piece of hydrophilic carbon cloth was used as additional GDL at the cathode side. The cathode was a Pt/graphene or a Pt/C electrode, while stacked SSMs were used as anode in all the investigated AELs. Before use, the SSMs were cleaned with IPA/EtOH (1:1 vol/vol) and distilled water and dried using an air stream. The cell components were compressed during cell assembling to realize the (quasi) zero-gap AEL configurations.

2.8. Alkaline electrolyzer characterization

The AELs were connected to a custom-built station. The anodic and cathodic compartments were fed with 30 wt% KOH solution through a peristaltic pump (Masterflex L/S Series). The electrolyte flow rate was 30 mL min^{-1} cm^{-2}. The electrolyte temperature was 80 °C, as controlled with a proportional-integral derivative controller. The AELs operated at atmospheric (1 bar) system pressure with separate electrolyte cycles. The latter avoids mixing of the anodic and cathodic electrolytes [52]. Thus, the anodic hydrogen contamination is limited, ensuring a safe AEL operation without requiring extra gas separating unit to reduce the crossover or the hydrogen content within the anodic half-cell [52]. The AELs were powered by a potentiostat/galvanostat (VMP3, Biologic) equipped with an external high-current booster channel. Galvanostatic polarization curves were acquired through a multistep CP protocol. The cell voltage was averaged over 3 min of each current step to provide a point of the polarization curve. To follow recommended practices guaranteeing the reproducibility of the polarization curves [23], the AELs were preconditioned through 6 CV cycles between cell voltages of 1 V and 2 V at a voltage scan rate of 5 mV s^{-1}. The stability of the AELs was assessed by means of an accelerated stress test (AST). As similarly reported for other type of electrolyzers (*e.g.*, PEM-ELs) [53], our AST protocol consists of alternating current density steps of 1 A cm^{-2} and 0.05 A cm^{-2}. Each galvanostatic step was kept for 15 min for a total test

duration of 24 h. The voltage efficiency of the AELs was calculated assuming a Faradaic efficiency for the HER equal to 1, thereby:

$$\text{voltage efficiency} = E_{rev}/E_{cell}$$

in which E_{rev} (1.18 V) is the thermodynamic reversible voltage for water electrolysis, *i.e.*, the minimum voltage required for the onset of water electrolysis (at 80 °C and 1 bar), while E_{cell} is the cell voltage. To facilitate the comparison of the performance of our AEL with those reported in the literature, the following energy efficiency metrics were also calculated:

$$\text{energy efficiency}_{HHV} = (M_{H2} \times HHV)/\text{energy}_{input} = E^0_{th}/E_{cell}$$

and

$$\text{energy efficiency}_{LHV} = (M_{H2} \times LHV)/\text{energy}_{input} = 1.25/E_{cell}$$

in which HHV and LHV are the hydrogen higher and lower heating value (141.7 kJ g_{H2}^{-1} and 120 kJ g_{H2}^{-1}), respectively, M_{H2} is the hydrogen weight produced by the AEL, E^0_{th} is the thermoneutral voltage for the water electrolysis at standard temperature and pressure conditions (*i.e.*, 1.48 V), E_{cell} is the cell voltage, energy_{input} is the electric energy utilized to produce the hydrogen, calculated by multiplying the operating power of AEL by time. Energy_{input} neglects some energy input contributions, including the thermal energy input and the energy consumption from water peristaltic pumps. [54] Consequently, despite they permit a direct comparison with literature results, our energy efficiencies are approximated metrics of the industrial ones.

3. Results and discussion

Pt NPs were anchored to single-/few-layer flakes of graphene (Scheme 1) to follow the structural design for standard Pt/C catalysts. [55] In such a catalysts structure, carbon black (*e.g.*, Vulcan XC-72R) supports Pt NPs to provide high ECSA by avoiding Pt agglomeration while ensuring high electronic conductivity (2.8 S cm^{-1} for Vulcan XC-72R) [56] and efficient ion transport through the micro-/-mesoporous carbonaceous network.

3.1. Materials production

Graphene was produced through the industrial WJM exfoliation method (STEP 1a, Scheme 1) [39,57], which provides a massive production of single-/few-layer graphene flakes (production rate of ~0.4 g min^{-1} on a single WJM apparatus) and a ~100% exfoliation yield (defined as the ratio between the weight graphitic flakes and the one of the initial graphite). Fig. 1a,b reports the BF-TEM and AFM images of representative WJM-produced graphene flakes, which have a flat morphology and irregular shapes. Lateral size and thickness data follow log-normal distributions (Fig. 1c,d), peaking at 990 and 2.5 nm, respectively, indicating the main presence of single/few-layer graphene flakes. Fig. 1e shows a Raman spectrum of the WJM-produced graphene sample, compared to that of starting graphite, normalized to the G peak. The spectra show the characteristic peaks of graphene and graphite (*i.e.*, G, D, D' and second-order peaks, namely 2D and D + D') [58,59]. As discussed in previous literature, in the $I(2D_1)/I(G)$ vs. $I(2D_2)/I(G)$ plot (Fig. 1f, I(X) denotes the intensity of the peak X), the data that fall above the line $I(2D_2) = I(2D_1)$ correspond to flakes with less than 5 layers, while those below that line refer to flakes with more than 5 layers (spectroscopically indistinguishable from graphite) [60,61]. Thus, our data confirmed the single-/few-layer structure of the WJM-produced flakes. In addition, I(D)/I(G) does not correlate with FWHM(G) (Fig. 1g), which means that the flakes do not have structural defects located on their basal plane [62,63]. The Pt NPs were synthesized *via* a facile, scalable and eco-friendly method (STEP 1b, Scheme 1) that produces size-tuneable spherical NPs without relying on the use of catalyst-poisoning reagents/organic coatings [43,44]. In fact, Pt NPs were stabilized in the water-based graphene dispersion through weakly bound citrate molecules that act as stabilizing agents in polar media [46], as proved by the negative ζ potential of the citrate-coated Pt NPs dispersion (Table S1). Recently, the binding modes of various carboxylate-containing systems on PGM surfaces have been extensively examined and it has been found that citrate ions exhibit three different binding modes to the PGM surface. [64] Fig. 1h shows a BF-TEM image of citrate-coated Pt NPs, which feature a spherical shape with an average diameter of 4.1 ± 0.6 nm (Fig. 1i). The Pt NPs were then mixed with graphene flakes (STEP 2, Scheme 1), and the citrate coating of the Pt NPs was easily removed by increasing the pH through NaOH addition (STEP 3, Scheme 1) [45], without recurring to harsh surface cleaning procedures [65]. Indeed, the alkalinity of the system causes the transformation of monodentate citrate ion into tetradentate-coordinated trisodium citrate [66]. The electrostatic repulsion between highly charged citrate molecules causes the detachment of citrate molecules, subsequently leading to the deposition of the Pt NPs on the target support [67], *i.e.*, graphene, without requiring complex/time-consuming immobilization processes [43]. This mechanism is supported by the increase of the ζ potential of the citrate-coated Pt NPs after the addition of 1 M NaOH (Table S1). A nearly complete precipitation of Pt NPs was observed after 1 h (Fig. S1). Also, the ζ potential of the native graphene dispersion in water:EtOH (80:20 vol/vol, see Experimental section) is negative (−47.1 mV, see Table S1), indicating a negatively charged graphene surface, which is consistent with previous studies [61,62]. During STEP 3, the addition of NaOH in the water-diluted graphene

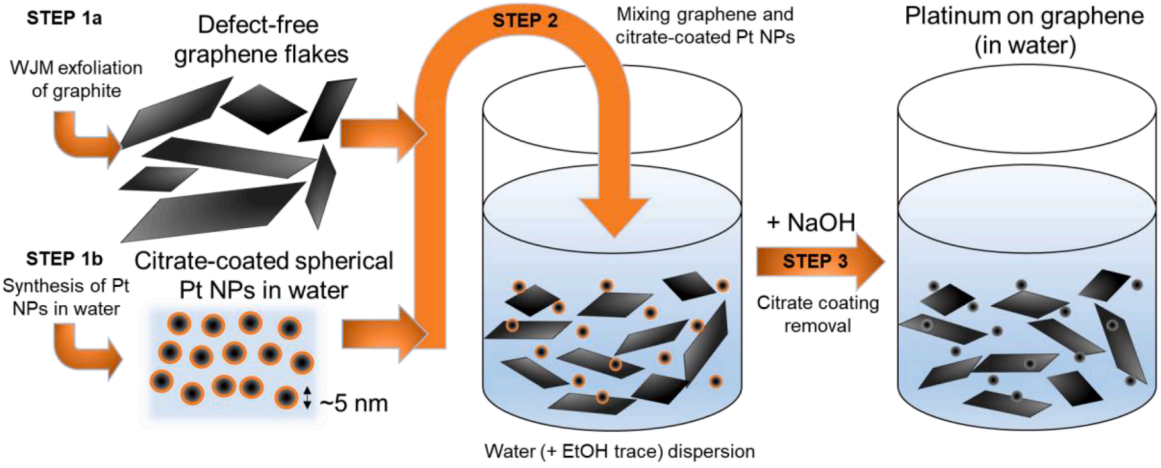

Scheme 1. Schematic representation of the Pt/graphene catalysts production.

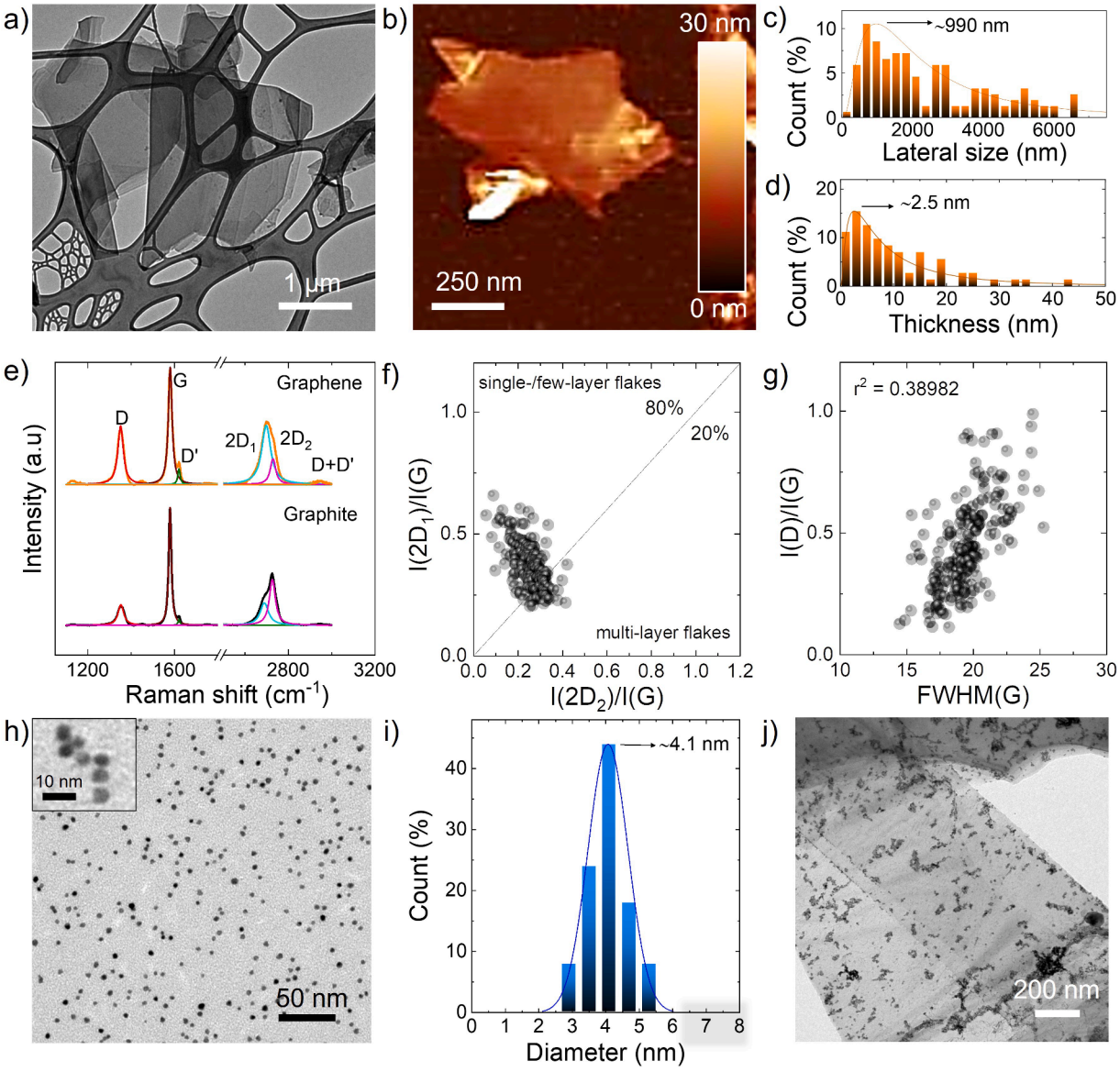

Fig. 1. (a) BF-TEM and (b) AFM images of the WJM-produced graphene flakes. (c) BF-TEM statistical analysis of the lateral size of the graphene flakes (146 flakes). (d) AFM statistical analysis of the thickness of the graphene flakes (103 flakes). (e) Raman spectra of the WJM-produced graphene flakes and native graphite powder (the batch of the latter was used for parallel works, and its Raman spectra is representative). (f) $I(2D_1)/I(G)$ vs. $I(2D_2)/I(G)$ and (g) I(D)/I(G) vs. FWHM(G) plots for the WJM-produced graphene flakes. The dashed line $I(2D_1) = I(2D_2)$ represents the multilayer condition (~5 layers). (h) BF-TEM image of citrate-coated Pt NPs. (i) BF-TEM statistical analysis of the diameter of the Pt NPs. (j) BF-TEM image of Pt/graphene catalysts.

dispersion further promotes the deprotonated state of graphene, favouring a robust anchoring of Pt NPs during the precipitation of the latter, as previously observed for positively charged molecules [61]. Importantly, the defect-free graphene structure guarantees an optimal control of the Pt NP anchoring, which is instead uncontrolled in defective carbon because of the enhanced reactivity of functional groups compared to the sp^2 lattice of pristine graphene [68–70]. In addition, the 2D morphology of the graphene flakes intrinsically acts as a physical barrier against the movement of the Pt NPs, which are therefore optimally trapped by graphene, avoiding precipitation losses. Fig. 1j shows the BF-TEM images of the Pt/graphene, evidencing that Pt NPs are homogeneously distributed over the surface of the graphene flakes, acting as effective Pt NPs-anchoring conductive supports.

3.2. Electrochemical characterization of the Pt/graphene

Cyclic voltammetry measurements in 1 M KOH were carried out to estimate the ECSA of Pt/graphene deposited on RDE coated through the H_{UPD} method [49,50]. As shown in Fig. 2a, the recorded CV curves of Pt/graphene exhibit a voltammetric profile associated to a poly-oriented Pt surface. In the high-potential region (>0.5 V vs. RHE), the peaks are associated to the oxidation/reduction of Pt surface towards Pt-OH and Pt-oxides, which concomitantly form with the specific adsorption of anions. [71] The peaks at +0.25 V vs. RHE and +0.36 V vs. RHE in the hydrogen ad-/desorption region are associated to an exchange between hydrogen and co-adsorbed hydroxide and water at the Pt(110) and Pt (100) facets [72,73] respectively, while the broad band underlying the peaks is generally attributed to the hydrogen adsorption on Pt(111)-like terrace [74], as well as cation adsorption and OH desorption [73,75]. Compared to typical voltammograms of Pt in acidic media, the hydrogen adsorption/desorption peaks are found at more positive potential (vs. RHE), in agreement with the non-Nernstian pH-dependence of the hydrogen binding energy for the Pt(110) and Pt(100) facets [76,77]. By analysing $Q_{H\text{-upd}}$ in the hydrogen adsorption region (see Experimental

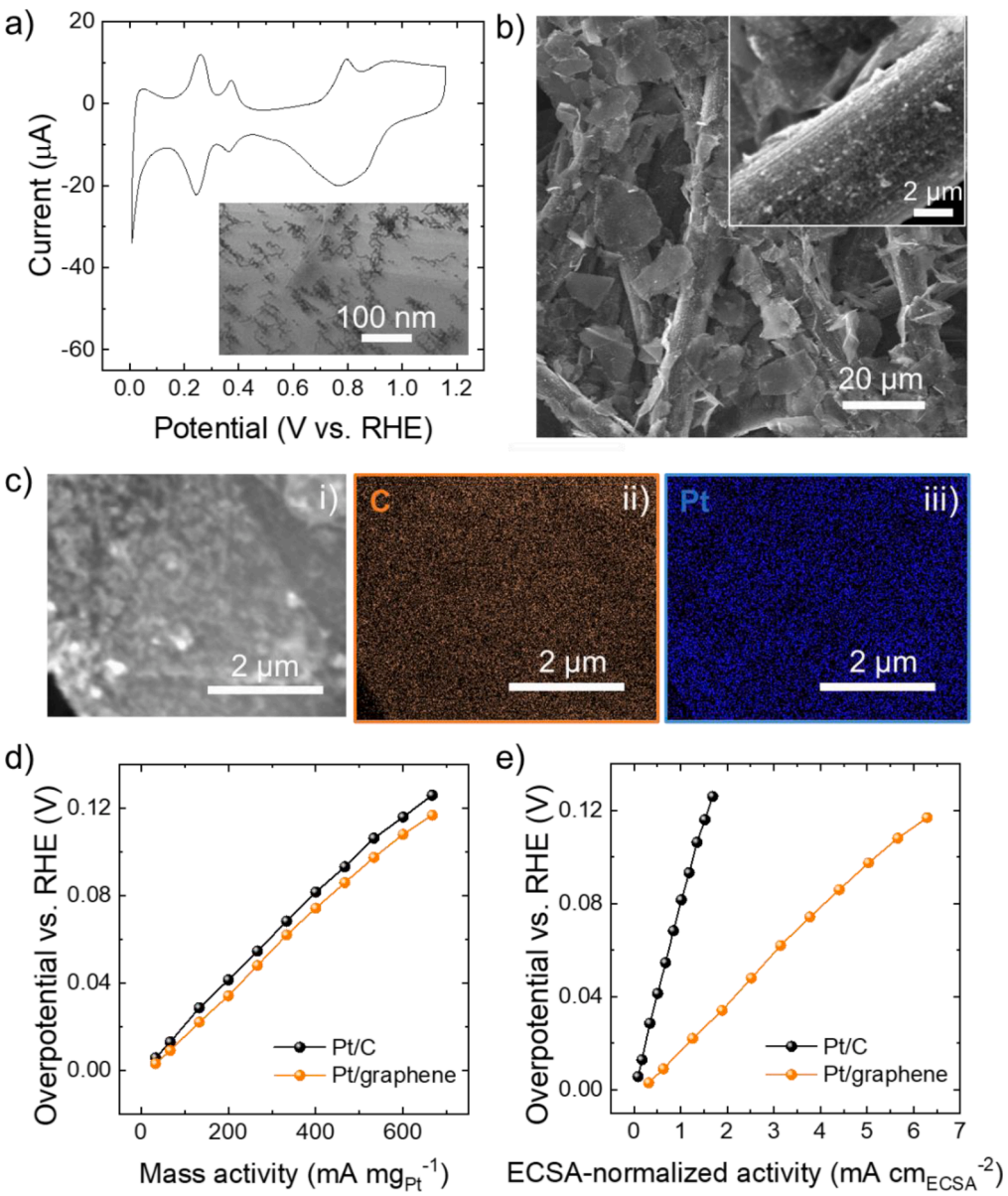

Fig. 2. (a) RDE curve measured for Pt/graphene catalysts in 1 M KOH (50th CV scan, potential scan rate = 50 mV s^{-1}). Inset panel shows the BF-TEM image of the Pt/graphene catalysts after the H_{UPD} characterization. (b) Top-view SEM image of Pt/graphene electrode consisting of a sprayed Pt/graphene catalysts coating on CPR substrate. The inset panel shows a SEM image of Pt/graphene electrode with increased magnification compared to that of the main panel. (c) SEM-EDS analysis of Pt/graphene electrodes. Panel (i): SEM image; panel (ii): C EDS-map; panel (iii) Pt EDS-map. (d) Mass activity and (e) ECSA-normalized activity (ECSA estimated by H_{UPD} method) measured for Pt/graphene and commercial Pt/C electrodes. Pt/C electrode was also evaluated in a parallel study (see ref. [20]).

section), the $mass_{Pt}$-normalized ECSA of our Pt/graphene was estimated to be 10.6 m^2 g_{Pt}^{-1}. This value is consistent with those reported for sub-10 nm Pt NPs [77]. Importantly, when Pt/graphene was redispersed in EtOH through ultrasonication, the Pt NPs were still anchored to the graphene surface (inset of Fig. 2a), indicating that the interaction between graphene and Pt NPs is preserved after the operation of the catalysts in alkaline media. Fig. S2a reports the CV curves obtained for commercial Pt/C catalysts, whose $mass_{Pt}$-normalized ECSA was found to be 39.5 m^2 g_{Pt}^{-1}, in accordance with the small diameter (<3 nm) of their Pt NPs (see BF-TEM image in Fig. S2b). Noteworthy, considering their different synthesis methods, the specific facets exposed by our Pt NPs and by the Pt particles in the commercial Pt/C catalyst may also differ substantially, leading to different ECSA-normalized activities, as shown hereafter. The as-produced aqueous dispersion of Pt/graphene was then spray coated onto CPR to produce a cathode for AELs with a m_{Pt} of ~300 μg cm^{-2}, as confirmed by ICP-EOS measurements. This m_{Pt} is similar or even inferior to those used in cathodes for high-performance electrolyzers operating either in alkaline [10,12–16] or acidic media [78,79]. As shown in Fig. 2b, Pt/graphene catalysts cover the graphitic fibres of the CPR. Thanks to their 2D morphology, Pt/graphene catalysts are trapped by the CPR fiber tangle. Consequently, we initially speculate that Pt/graphene forms a surface coating that can minimize the distance of the catalytic site from the diaphragm of a zero-gap AELs, while avoiding catalysts detachment if Pt NPs are anchored to the graphene surface, as supported by ζ potential measurements. Notably, since CPR acts like a filter during the deposition of Pt/graphene *via* spray coatings, in the SEM image reported in Fig. 2b, the biggest flakes, with lateral dimension higher than 5 μm, stands out. Their presence, however, has been found to be marginal by the BF-TEM analysis of the WJM-produced sample (see Fig. 1c). By increasing the magnification of the SEM image (inset panel of Fig. 2b), the flakes with smaller lateral sizes (*e.g.*, ≤ 1 um) are also evidenced over the CPR fibres, showing their pronounced presence, which is consistent with our BF-TEM analysis (Fig. 1c). Contrary to Pt/graphene, previous literature indicated that Pt/C can instead infiltrate porous CPR when the catalyst size is inferior to that of the substrate pores, leading to a progressive loss of the catalytic materials during both electrode preparation and operation [80,81]. As shown in Fig. S2b, in Pt/C, carbon black particles have an average diameter well below 100 nm, which is significantly lower than the average lateral size of our WJM-produced graphene flakes (see Fig. 1c). Fig. 2c shows the

SEM-EDS analysis (SEM image and the corresponding C and Pt EDS maps) of the Pt/graphene electrode, for which we found a Pt:C weight ratio of 0.23, near the expected one of 0.2. The Pt/graphene cathode was first evaluated in a three-electrode cell configuration, by acquiring its galvanostatic polarization curves, following the practices recommended for nanostructured electrodes [49,82–85]. To evaluate the intrinsic activity of our Pt/graphene compared to commercial Pt/C (deposited on CPR with m_{Pt} of ~300 μg cm^{-2}, as described in a parallel study, see ref. [20]), the cathodic current of our electrodes was normalized on m_{Pt} (mass activity of Pt -MA_{Pt}-) or ECSA of our Pt NPs (ECSA-normalized activity). Compared to Pt/C, Pt/graphene shows a slightly superior MA_{Pt} towards the HER, reaching ~540 mA mg_{Pt}^{-1} at the HER overpotential (vs. RHE) of 0.1 V (Fig. 2d). Being m_{Pt} the same in Pt/graphene and Pt/C, the geometric activity (*i.e.*, the geometric area-normalized cathodic current vs. overpotential) of our electrodes reflects the MA_{Pt} of our electrodes. To refer to an operating (geometric) current density condition approaching that of AELs (*i.e.*, hundreds of mA cm^{-2}), the overpotential (vs. RHE) at 100 mA cm^{-2} (η_{100}) was used as a catalytic activity metric. As shown in Fig. S3, our Pt/graphene featured a η_{100} of 0.062 V, lower than that of Pt/C (0.068 V) and approaching the performances achieved with PGM-based catalysts (*e.g.*, PGM-transition metal alloys or metal single atoms) in acidic media [34,86]. Interestingly, the

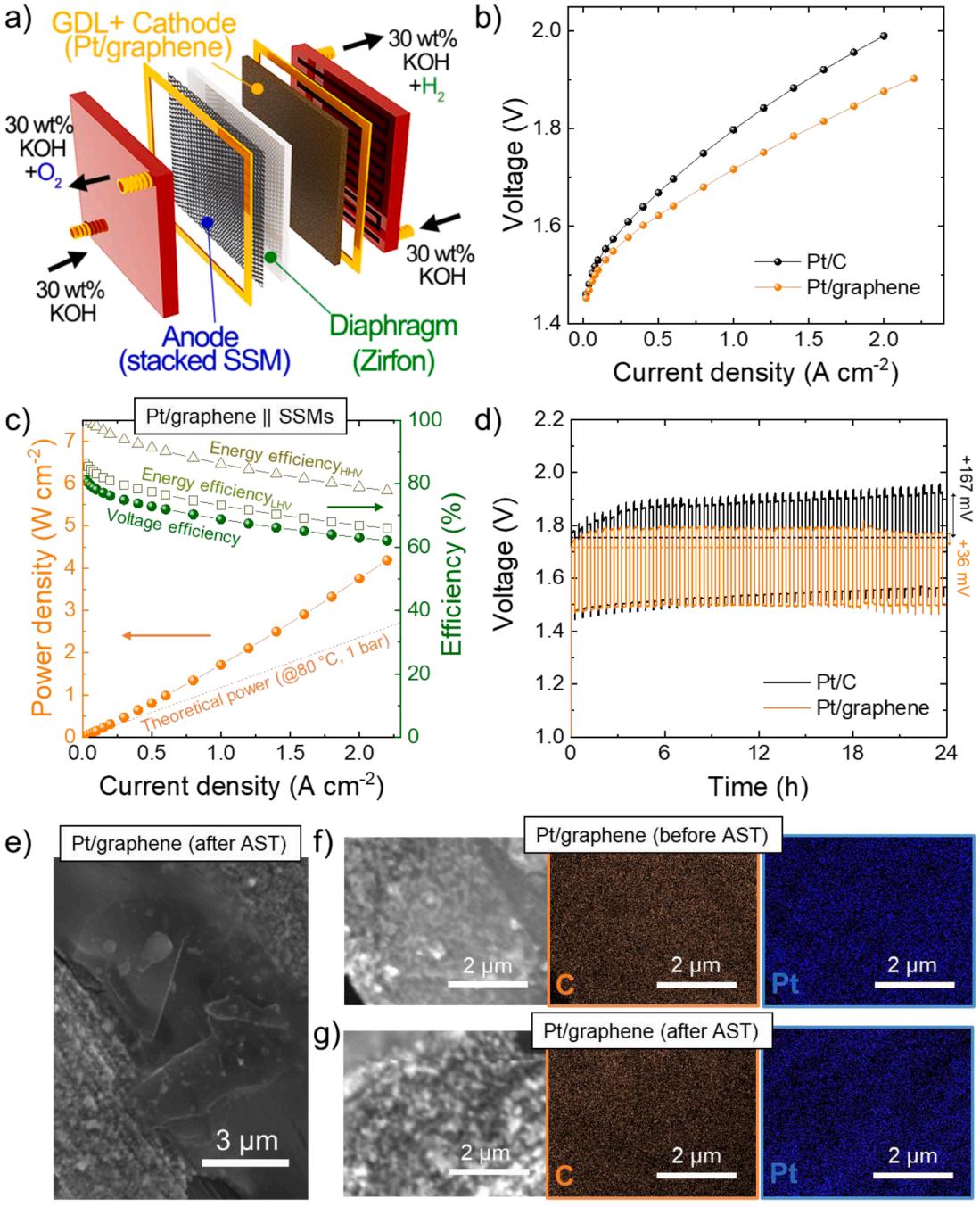

Fig. 3. (a) Sketch of our AEL configurations, using Pt/graphene or Pt/C cathode, stacked SSMs anode (no GDL) and Zirfon UTP 220 diaphragm. Operating conditions: 30 wt% KOH electrolyte; atmospheric pressure (1 bar); 80 °C temperature. Reference AEL based on Pt/C was also investigated in a parallel study, see ref. [20]. (b) Galvanostatic polarization curves measured for the AELs based on Pt/graphene or Pt/C cathodes (m_{Pt} ~300 μg cm^{-2}) and (c) Power density and efficiency of Pt/graphene || SSMs AELs as a function of the current density. (d) 24 h-ASTs for Pt/graphene||SSMs and Pt/C||SSMs AELs. (e) Comparison between SEM image of Pt/graphene cathode after 24 h-AST. (f) SEM-EDS analysis of Pt/graphene electrode before and g) after the 24 h-AST of its corresponding AEL.

ECSA-normalized activity of Pt/graphene is significantly superior to that of Pt/C (Fig. 2e). As suggested by the different shapes of the CV curves in the H_{UPD} region measured for our Pt NPs and those in Pt/C (Fig. 2a and Fig. S2, respectively), the higher ECSA-normalized activity of our Pt NPs compared to those in Pt/C may be due to their different structural characteristics, which may also regard the Pt facets exposure [87]. Furthermore, the Pt NPs interaction with graphene (thus, sp^2 C) can also promote the reduction of adsorbed H^+ and accelerate the H_2 desorption more favourably than the interaction between Pt and carbon black (including sp^3 C) [88]. Potentiodynamic LSV curves (Fig. S4) also confirmed the activity trends retrieved from the galvanostatic polarization curves, even though other possible reactions, *e.g.*, hydrogen adsorption, and double-layer charging can lead to inaccurate determination of activity metrics, especially at low HER-overpotentials [49, 82–85].

3.3. Pt/graphene-based AEL performances

After assessing their HER-activity in the three-electrode cell configuration, Pt/graphene electrodes were further evaluated as cathodes in atmospheric AELs operating with 30 wt% KOH aqueous electrolyte at 80 °C. Indeed, three-electrode cell configuration tests are not sufficient to assess the performance and stability of our electrode in the AEL operating conditions [23,89–91], which include mechanical stresses associated to cell torque, electrolyte circulation and pronounced gas bubbling [23], as well as temperature and electrolyte concentration higher than those commonly used at electrode-level characterization [4].

Single-cell AELs were assembled by pairing either Pt/graphene or Pt/C cathodes with stacked SSM-based anodes (Fig. 3a). Stainless-steel has been recently established as inexpensive catalysts for the oxygen evolution reaction (OER) with robust performances [92–94] even under fluctuating potentials (*e.g.*, those occurring during AEL shutdowns [95] or when AEL are powered by renewable sources [96]), that cause repeated oxidation and reduction of catalysts [97,98]. Zirfon PERL UTP 220 membrane was used as a diaphragm with low ohmic areal resistance (~0.1 Ω cm^{-2}) [99] and limited hydrogen crossover (anodic hydrogen content typically < 2%, <0.2% at operating current density ≥ 500 mA cm^{-2}) when operating at pressures lower than 20 bar [99]. The so-realized AELs are herein after labeled as cathode||SSMs, where the cathode is either Pt/graphene or Pt/C. Fig. 3b shows the galvanostatic polarization curves measured for the investigated AELs. Pt/graphene||SSMs outperformed Pt/C||SSMs (as tested in a parallel study, see ref. [20]), reaching 0.5 A cm^{-2}, 1 A cm^{-2} and 2 A cm^{-2} at 1.62 V, 1.71 V and 1.88 V, respectively, which is consistent with the superior HER-activity (measured in three-electrode cell configuration) of Pt/graphene compared to Pt/C. Moreover, after acquiring the galvanostatic polarization curve for the Pt/C||SSMs, the catholyte changed color, showing a darkening attributed to a pronounced Pt/C catalysts detachment. This effect was not observed for the Pt/graphene||SSMs configuration. Thus, the progressive loss of catalysts in Pt/C could also degrade the AEL performance during the galvanostatic measurements, indicating that a suitable binder must be incorporated into the cathode formulation, as known from literature reporting other type of electrolyzer technologies [21,22]. In contrast, Pt/graphene operated robustly even in absence of additional binders, preventing the latter from passivating the catalytic sites of the catalysts. Consequently, as shown in Fig. 3c, our Pt/graphene||SSMs operated with voltage efficiency of 72.8%, 68.8% and 62.9% at 0.5 A cm^{-2}, 1 A cm^{-2} and 2 A cm^{-2}, respectively. These voltage efficiencies correspond to energy $efficiency_{HHV}$ of 91.3%, 86.2% and 78.9% (energy $efficiency_{LHV}$ of 77.1%, 72.8% and 66.6%), respectively. These performances approach those reported for the most efficient electrolyzers, including AEM-ELs and PEM-ELs (see Table S2). To assess further the robustness of our Pt/graphene cathode, its corresponding AEL was tested through a 24 h-AST protocol consisting of alternating galvanostatic steps between 1 A cm^{-2} and 0.05 A cm^{-2}, with each galvanostatic step kept for 15 min. As shown in Fig. 3d, Pt/graphene||SSMs exhibited a nearly stable voltage at 1 A cm^{-2}, leading to a voltage increase as low as +36 mV at the end of the test. Conversely, Pt/C||SSMs featured a voltage increase of +190 mV, confirming the Pt/C instability previously observed during the polarization curve test. To quantify the retention of the catalysts in our AEL cathodes during operation, SEM-EDS analysis of the investigated cathodes was conducted after the ASTs. As shown in Fig. 3e, after the AST, Pt/graphene still showed flakes of graphene trapped within CPR fibers, similarly to the as-produced electrode (Fig. 2b). This supports our findings that, thanks to their 2D morphology, Pt-anchoring graphene flakes are hardly detached from the electrode, being filtered by CPR fibers. In addition, the elemental EDS maps show that the Pt was still homogeneously distributed over C after the AST (Fig. 3f), revealing a Pt weight retention approaching 100% (see SEM-EDS analysis of the as-produced electrode in Fig. 2c). Differently, for the Pt/C cathode, electrode materials massively detached and dispersed into the electrolyte (Pt weight retention as low as 21%) (Fig. S5), indicating that, in the absence of a suitable binding agent, Pt NPs deposited onto carbon black aggregates can move through the pores of the CPR substrate (the overall size of the aggregates is <100 nm). Overall, our results confirmed that graphene can be used as an ideal support for Pt NPs for the realization of advanced binder-free cathodes for AELs.

4. Conclusions

In summary, we reported that graphene, produced through an industrial liquid-phase exfoliation method, *i.e.*, WJM exfoliation of natural graphite, can be used as ideal support for Pt NPs acting as catalysts for alkaline HER. Platinum NPs were synthesized *via* a facile method in an aqueous environment that does not rely on surface-poisoning reagents (*e.g.*, shape-directing agents like poly(vinylpyrrolidone), tetradecyl trimethyl ammonium bromide, cetyltrimethylammonium bromide and hexadecylpyridinium bromide, commonly used for the synthesis of nanocrystals), leading to a citrate-capped Pt NPs. Once these NPs are supported on our WJM-produced graphene flakes in water dispersion, the removal of their citrate coating through NaOH addition promotes a chemical interaction of surface-cleaned Pt NPs and graphene flakes, resulting in Pt/graphene catalysts. The as-produced catalysts can then be deposited onto conventional support acting as GDLs by means of large-area printing/coating techniques. Thus, Pt/graphene catalysts were sprayed on conventional CPR substrates, realizing binder-free cathodes for AELs. In terms of HER-activity, our Pt/graphene cathodes outperform benchmark Pt/C, resulting in AELs operating with current densities of 0.5 A cm^{-2}, 1 A cm^{-2} and 2 A cm^{-2} at voltages of 1.62 V, 1.71 and 1.88 V, respectively. These performances correspond to energy efficiencies (based on the hydrogen HHV) of 91.3%, 86.2% and 78.9%, respectively, approaching the record high-values present in the literature for competing technologies, including AEM-ELs and PEM-ELs. In addition, the Pt-anchoring 2D morphology of graphene guarantees that the catalysts are trapped within CPR fibres, preventing the electrode material detachment even in absence of any polymeric binder. On the contrary, Pt/C cathodes showed a pronounced electrode material loss associated to the small size of carbon black aggregates, which can move through the pores of the CPR, thus detaching from the substrate during the AEL operation. Overall, our results prove that graphene can represent an ideal support for catalytic nanoparticles for the realization of advanced binder-free (or low-binder content) electrodes with superior performance in AELs. The absence of binder intrinsically avoids the insulation of the cathode catalytic sites, while the 2D morphology of the graphene blocks the Pt detachment, ensuring stable AEL performances. We can anticipate the on-going works from our groups indicating that the capital expenses of an ideal MW-scale system based on high-performance single cells using Pt/C cathode are marginally affected by m_{Pt} (considering values on the order of 100 μg cm^{-2}) for single cell current density of about 1 A cm^{-2}. Considering the importance to

minimize the operating expense by maximizing the AEL performances over time, it is therefore crucial to consolidate AEL systems capable to operate at a high current density well above those of traditional systems (*e.g.*, $\leq$400 A cm^{-2}). In this scenario, the use of Pt/graphene cathodes can potentially reduce the overall H_2 production cost of the AEL plants based on Pt/C cathode, supporting the achievement of worldwide 2030 targets (<\$2.5 kg_{H2}^{-1}) [100].

CRediT authorship contribution statement

Marilena Isabella Zappia: Methodology, Investigation, Data curation. **Valentina Mastronardi:** Methodology, Investigation, Data curation. **Sebastiano Bellani:** Conceptualization, Methodology, Investigation, Data curation, Writing – original draft. **Yong Zuo:** Visualization, Methodology, Investigation. **Gabriele Bianca:** Visualization, Methodology, Investigation. **Luca Gabatel:** Methodology, Investigation. **Matteo Gentile:** Methodology, Investigation. **Ahmad Bagheri:** Methodology, Investigation. **Hossein Beydaghi:** Methodology, Investigation. **Filippo Drago:** Methodology, Investigation. **Michele Ferri:** Methodology, Investigation, Validation. **Mauro Moglianetti:** Methodology, Investigation. **Pier Paolo Pompa:** Supervision, Writing – review & editing. **Liberato Manna:** Supervision, Conceptualization, Writing – review & editing. **Francesco Bonaccorso:** Supervision, Conceptualization, Writing – review & editing.

Declaration of Competing Interest

The authors declare the following financial interests/personal relationships which may be considered as potential competing interests:

Francesco Bonaccorso reports financial support was provided by European Commission

Data availability

Data will be made available on request.

Acknowledgements

This work has received funding from the European Union's Horizon 2020 "Proof of Concept" program under Grant Agreement No. 899412 (HyCat); the European Union's Horizon 2020 research and innovation program under Grant Agreement No. 881603- GrapheneCore3; the European Union's SENSIBAT project under Grant Agreement No. 957273; the Italian Ministry of Foreign Affairs and International Cooperation (MAECI) through Cooperation Project "GINGSENG" (Grant PGR05249) between Italy and China.

Supplementary materials

Supplementary material associated with this article can be found, in the online version, at doi:10.1016/j.electacta.2023.142696.

References

[1] Innovation Trends in Electrolysers for Hydrogen Production, IRENA, 2022. https://www.irena.org/publications/2022/May/Innovation-Trends-in-Electrolysers-for-Hydrogen-Production.
[2] Z. Yan, J.L. Hitt, J.A. Turner, T.E. Mallouk, Renewable electricity storage using electrolysis, Proc. Natl. Acad. Sci. 117 (2020) 12558–12563, https://doi.org/10.1073/pnas.1821686116.
[3] T. Smolinka, E.T. Ojong, J. Garche, Chapter 8 - Hydrogen production from renewable energies-Electrolyzer technologies. Electrochemical Energy Storage for Renewable Sources and Grid Balancing, 2015, pp. 103–128, https://doi.org/10.1016/B978-0-444-62616-5.00008-5.
[4] A. Buttler, H. Spliethoff, Current status of water electrolysis for energy storage, grid balancing and sector coupling via power-to-gas and power-to-liquids: a review, Renew. Sustain. Energy Rev. 82 (2018) 2440–2454, https://doi.org/10.1016/j.rser.2017.09.003.
[5] Cost Forecast for Low Temperature Electrolysis - Technology Driven Bottom-Up Prognosis for PEM and Alkaline Water Electrolysis, Fraunhofer, 2021. https://www.ise.fraunhofer.de/content/dam/ise/de/documents/publications/studies/cost-forecast-for-low-temperature-electrolysis.pdf.
[6] M. Schalenbach, G. Tjarks, M. Carmo, W. Lueke, M. Mueller, D. Stolten, Acidic or Alkaline? Towards a new perspective on the efficiency of water electrolysis, J. Electrochem. Soc. 163 (2016) F3197–F3208, https://doi.org/10.1149/2.0271611jes.
[7] J.W. Lee, J.H. Lee, C. Lee, H.S. Cho, M. Kim, S.K. Kim, J.H. Joo, W.C. Cho, C. H. Kim, Cellulose nanocrystals-blended zirconia/polysulfone composite separator for alkaline electrolyzer at low electrolyte contents, Chem. Eng. J. 428 (2022), 131149, https://doi.org/10.1016/j.cej.2021.131149.
[8] Platinum Group Metal Catalysts: supply chain deep dive assessment, U.S. Department of Energy, 2022, https://www.energy.gov/sites/default/files/2022-02/PGM%20catalyst%20supply%20chain%20report%20-%20final%20draft%202.25.22.pdf.
[9] J. Wang, Y. Gao, H. Kong, J. Kim, S. Choi, F. Ciucci, Y. Hao, S. Yang, Z. Shao, J. Lim, Non-precious-metal catalysts for alkaline water electrolysis: operando characterizations, theoretical calculations, and recent advances, Chem. Soc. Rev. 49 (2020) 9154–9196, https://doi.org/10.1039/D0CS00575D.
[10] H. Koshikawa, H. Murase, T. Hayashi, K. Nakajima, H. Mashiko, S. Shiraishi, Y. Tsuji, Single nanometer-sized NiFe-layered double hydroxides as anode catalyst in anion exchange membrane water electrolysis cell with energy conversion efficiency of 74.7% at 1.0 A cm^{-2}, ACS Catal. 10 (2020) 1886–1893, https://doi.org/10.1021/acscatal.9b04505.
[11] N. Chen, S.Y. Paek, J.Y. Lee, J.H. Park, S.Y. Lee, Y.M. Lee, High-performance anion exchange membrane water electrolyzers with a current density of 7.68 A cm^{-2} and a durability of 1000 hours, Energy Environ. Sci. 14 (2021) 6338–6348, https://doi.org/10.1039/D1EE02642A.
[12] R.I. Masel, Z. Liu, S. Sajjad, Anion exchange membrane electrolyzers showing 1 A/cm^2 at less than 2 V, ECS Trans. 75 (2016) 1143–1146, https://doi.org/10.1149/07514.1143ecst.
[13] Z. Liu, S.D. Sajjad, Y. Gao, J. Kaczur, R. Masel, An alkaline water electrolyzer with Sustainion™ membranes: 1 A/cm^2 at 1.9 V with base metal catalysts, ECS Trans. 77 (2017) 71–73, https://doi.org/10.1149/07709.0071ecst.
[14] M.S. Cha, J.E. Park, S. Kim, S.H. Han, S.H. Shin, S.H. Yang, T.H. Kim, D.M. Yu, S. So, Y.T. Hong, S.J. Yoon, S.G. Oh, S.Y. Kang, O.H. Kim, H.S. Park, B. Bae, Y. E. Sung, Y.H. Cho, J.Y. Lee, Poly(carbazole)-based anion-conducting materials with high performance and durability for energy conversion devices, Energy Environ. Sci. 13 (2020) 3633–3645, https://doi.org/10.1039/D0EE01842B.
[15] J. Xiao, A.M. Oliveira, L. Wang, Y. Zhao, T. Wang, J. Wang, B.P. Setzler, Y. Yan, Water-fed hydroxide exchange membrane electrolyzer enabled by a fluoride-incorporated nickel-iron oxyhydroxide oxygen evolution electrode, ACS Catal. 11 (2021) 264–270, https://doi.org/10.1021/acscatal.0c04200.
[16] D. Li, E.J. Park, W. Zhu, Q. Shi, Y. Zhou, H. Tian, Y. Lin, A. Serov, B. Zulevi, E. D. Baca, C. Fujimoto, H.T. Chung, Y.S. Kim, Highly quaternized polystyrene ionomers for high performance anion exchange membrane water electrolysers, Nat. Energy 5 (2020) 378–385, https://doi.org/10.1038/s41560-020-0577-x.
[17] https://www.miningweekly.com/article/pgms-playing-atypical-role-in-alkaline-electrolyser-lowering-green-hydrogen-cost-outlook-2021-10-26 (accessed on 23/04/2022).
[18] M.K. Cho, H.Y. Park, H.J. Lee, H.J. Kim, A. Lim, D. Henkensmeier, S.J. Yoo, J. Y. Kim, S.Y. Lee, H.S. Park, J.H. Jang, Alkaline anion exchange membrane water electrolysis: effects of electrolyte feed method and electrode binder content, J. Power Sources 382 (2018) 22–29, https://doi.org/10.1016/j.jpowsour.2018.02.025.
[19] A. Hodges, A.L. Hoang, G. Tsekouras, K. Wagner, C.Y. Lee, G.F. Swiegers, G. G. Wallace, A high-performance capillary-fed electrolysis cell promises more cost-competitive renewable hydrogen, Nat. Commun. 13 (2022) 1304, https://doi.org/10.1038/s41467-022-28953-x.
[20] M.I. Zappia, S. Bellani, Y. Zuo, M. Ferri, F. Drago, L. Manna, F. Bonaccorso, High-current density alkaline electrolyzers: the role of Nafion binder content in the catalyst coatings and techno-economic analysis, Front. Chem. 10 (2022), https://doi.org/10.3389/fchem.2022.1045212. https://www.frontiersin.org/articles/10.3389/fchem.2022.1045212.
[21] M. Plevová, J. Hnát, J. Žitka, L. Pavlovec, M. Otmar, K. Bouzek, Optimization of the membrane electrode assembly for an alkaline water electrolyser based on the catalyst-coated membrane, J. Power Sources 539 (2022), 231476, https://doi.org/10.1016/j.jpowsour.2022.231476.
[22] S. Koch, P.A. Heizmann, S.K. Kilian, B. Britton, S. Holdcroft, M. Breitwieser, S. Vierrath, The effect of ionomer content in catalyst layers in anion-exchange membrane water electrolyzers prepared with reinforced membranes (Aemion +™), J. Mater. Chem. A 9 (2021) 15744–15754, https://doi.org/10.1039/D1TA01861B.
[23] C. Karacan, F.P. Lohmann-Richters, G.P. Keeley, F. Scheepers, M. Shviro, M. Müller, M. Carmo, D. Stolten, Challenges and important considerations when benchmarking single-cell alkaline electrolyzers, Int. J. Hydrog. Energy 47 (2022) 4294–4303, https://doi.org/10.1016/j.ijhydene.2021.11.068.
[24] B. Tan, N.L. Thomas, A review of the water barrier properties of polymer/clay and polymer/graphene nanocomposites, J. Membr. Sci. 514 (2016) 595–612, https://doi.org/10.1016/j.memsci.2016.05.026.
[25] K.S. Novoselov, V.I. Fal'ko, L. Colombo, P.R. Gellert, M.G. Schwab, K. Kim, A roadmap for graphene, Nature 490 (2012) 192–200, https://doi.org/10.1038/nature11458.

[26] X. Wang, C. Xu, M. Jaroniec, Y. Zheng, S.Z. Qiao, Anomalous hydrogen evolution behavior in high-pH environment induced by locally generated hydronium ions, Nat. Commun. 10 (2019) 4876, https://doi.org/10.1038/s41467-019-12773-7.

[27] F. Razmjooei, A. Farooqui, R. Reissner, A.S. Gago, S.A. Ansar, K.A. Friedrich, Elucidating the performance limitations of alkaline electrolyte membrane electrolysis: dominance of anion concentration in membrane electrode assembly, ChemElectroChem 7 (2020) 3951–3960, https://doi.org/10.1002/celc.202000605.

[28] I.T. McCrum, M.T.M. Koper, The role of adsorbed hydroxide in hydrogen evolution reaction kinetics on modified platinum, Nat. Energy 5 (2020) 891–899, https://doi.org/10.1038/s41560-020-00710-8.

[29] W. Sheng, H.A. Gasteiger, Y. Shao-Horn, Hydrogen oxidation and evolution reaction kinetics on platinum: acid vs alkaline electrolytes, J. Electrochem. Soc. 157 (2010) B1529, https://doi.org/10.1149/1.3483106.

[30] H. Jin, M. Ha, M.G. Kim, J.H. Lee, K.S. Kim, Engineering Pt coordination environment with atomically dispersed transition metal sites toward superior hydrogen evolution, Adv. Energy Mater. 13 (2023), 2204213, https://doi.org/10.1002/aenm.202204213.

[31] J.N. Tiwari, S. Sultan, C.W. Myung, T. Yoon, N. Li, M. Ha, A.M. Harzandi, H. J. Park, D.Y. Kim, S.S. Chandrasekaran, W.G. Lee, V. Vij, H. Kang, T.J. Shin, H. S. Shin, G. Lee, Z. Lee, K.S. Kim, Multicomponent electrocatalyst with ultralow Pt loading and high hydrogen evolution activity, Nat. Energy 3 (2018) 773–782, https://doi.org/10.1038/s41560-018-0209-x.

[32] J.N. Tiwari, N.K. Dang, S. Sultan, P. Thangavel, H.Y. Jeong, K.S. Kim, Multi-heteroatom-doped carbon from waste-yeast biomass for sustained water splitting, Nat. Sustain. 3 (2020) 556–563, https://doi.org/10.1038/s41893-020-0509-6.

[33] S. Sultan, M.H. Diorizky, M. Ha, J.N. Tiwari, H. Choi, N.K. Dang, P. Thangavel, J. H. Lee, H.Y. Jeong, H.S. Shin, Y. Kwon, K.S. Kim, Modulation of Cu and Rh single-atoms and nanoparticles for high-performance hydrogen evolution activity in acidic media, J. Mater. Chem. A 9 (2021) 10326–10334, https://doi.org/10.1039/D1TA01067K.

[34] N.K. Dang, M. Umer, P. Thangavel, S. Sultan, J.N. Tiwari, J.H. Lee, M.G. Kim, K. S. Kim, Surface enrichment of iridium on IrCo alloys for boosting hydrogen production, J. Mater. Chem. A 9 (2021) 16898–16905, https://doi.org/10.1039/D1TA02597J.

[35] C. Minke, M. Suermann, B. Bensmann, R. Hanke-Rauschenbach, Is iridium demand a potential bottleneck in the realization of large-scale PEM water electrolysis? Int. J. Hydrog. Energy 46 (2021) 23581–23590, https://doi.org/10.1016/j.ijhydene.2021.04.174.

[36] J. Gao, H. Tao, B. Liu, Progress of nonprecious-metal-based electrocatalysts for oxygen evolution in acidic media, Adv. Mater. 33 (2021), 2003786, https://doi.org/10.1002/adma.202003786.

[37] S. Bellani, A. Bartolotta, A. Agresti, G. Calogero, G. Grancini, A. Di Carlo, E. Kymakis, F. Bonaccorso, Solution-processed two-dimensional materials for next-generation photovoltaics, Chem. Soc. Rev. 50 (2021) 11870–11965, https://doi.org/10.1039/D1CS00106J.

[38] C. Backes, A.M. Abdelkader, C. Alonso, A. Andrieux-Ledier, R. Arenal, J. Azpeitia, N. Balakrishnan, L. Banszerus, J. Barjon, R. Bartali, S. Bellani, C. Berger, R. Berger, M.M.B. Ortega, C. Bernard, P.H. Beton, A. Beyer, A. Bianco, P. Bøggild, F. Bonaccorso, G.B. Barin, C. Botas, R.A. Bueno, D. Carriazo, A. Castellanos-Gomez, M. Christian, A. Ciesielski, T. Ciuk, M.T. Cole, J. Coleman, C. Coletti, L. Crema, H. Cun, D. Dasler, D. De Fazio, N. Díez, S. Drieschner, G.S. Duesberg, R. Fasel, X. Feng, A. Fina, S. Forti, C. Galiotis, G. Garberoglio, J.M. García, J. A. Garrido, M. Gibertini, A. Gölzhäuser, J. Gómez, T. Greber, F. Hauke, A. Hemmi, I. Hernandez-Rodriguez, A. Hirsch, S.A. Hodge, Y. Huttel, P.U. Jepsen, I. Jimenez, U. Kaiser, T. Kaplas, H. Kim, A. Kis, K. Papagelis, K. Kostarelos, A. Krajewska, K. Lee, C. Li, H. Lipsanen, A. Liscio, M.R. Lohe, A. Loiseau, L. Lombardi, M.F. López, O. Martin, C. Martín, L. Martínez, J.A. Martin-Gago, J. I. Martínez, N. Marzari, Á. Mayoral, J. McManus, M. Melucci, J. Méndez, C. Merino, P. Merino, A.P. Meyer, E. Miniussi, V. Miseikis, N. Mishra, V. Morandi, C. Munuera, R. Muñoz, H. Nolan, L. Ortolani, A.K. Ott, I. Palacio, V. Palermo, J. Parthenios, I. Pasternak, A. Patane, M. Prato, H. Prevost, V. Prudkovskiy, N. Pugno, T. Rojo, A. Rossi, P. Ruffieux, P. Samorì, L. Schué, E. Setijadi, T. Seyller, G. Speranza, C. Stampfer, I. Stenger, W. Strupinski, Y. Svirko, S. Taioli, K.B. K. Teo, M. Testi, F. Tomarchio, M. Tortello, E. Treossi, A. Turchanin, E. Vazquez, E. Villaro, P.R. Whelan, Z. Xia, R. Yakimova, S. Yang, G.R. Yazdi, C. Yim, D. Yoon, X. Zhang, X. Zhuang, L. Colombo, A.C. Ferrari, M. Garcia-Hernandez, Production and processing of graphene and related materials, 2D Mater. 7 (2020) 22001, https://doi.org/10.1088/2053-1583/ab1e0a.

[39] A.E. Del Rio Castillo, V. Pellegrini, A. Ansaldo, F. Ricciardella, H. Sun, L. Marasco, J. Buha, Z. Dang, L. Gagliani, E. Lago, N. Curreli, S. Gentiluomo, F. Palazon, M. Prato, R. Oropesa-Nuñez, P.S. Toth, E. Mantero, M. Crugliano, A. Gamucci, A. Tomadin, M. Polini, F. Bonaccorso, High-yield production of 2D crystals by wet-jet milling, Mater. Horiz. 5 (2018) 890–904, https://doi.org/10.1039/C8MH00487K.

[40] S. Bellani, B. Martín-García, R. Oropesa-Nuñez, V. Romano, L. Najafi, C. Demirci, M. Prato, A.E. Del Rio Castillo, L. Marasco, E. Mantero, G. D'Angelo, F. Bonaccorso, Ion sliding" on graphene: a novel concept to boost supercapacitor performance, Nanoscale Horiz. 4 (2019) 1077–1091, https://doi.org/10.1039/C8NH00446C.

[41] S. Bellani, L. Najafi, M. Prato, R. Oropesa-Nuñez, B. Martín-García, L. Gagliani, E. Mantero, L. Marasco, G. Bianca, M.I. Zappia, C. Demirci, S. Olivotto, G. Mariucci, V. Pellegrini, M. Schiavetti, F. Bonaccorso, Graphene-based electrodes in a vanadium redox flow battery produced by rapid low-pressure combined gas plasma treatments, Chem. Mater. 33 (2021) 4106–4121, https://doi.org/10.1021/acs.chemmater.1c00763.

[42] S. Pescetelli, A. Agresti, G. Viskadouros, S. Razza, K. Rogdakis, I. Kalogerakis, E. Spiliarotis, E. Leonardi, P. Mariani, L. Sorbello, M. Pierro, C. Cornaro, S. Bellani, L. Najafi, B. Martín-García, A.E. Del Rio Castillo, R. Oropesa-Nuñez, M. Prato, S. Maranghi, M.L. Parisi, A. Sinicropi, R. Basosi, F. Bonaccorso, E. Kymakis, A. Di Carlo, Integration of two-dimensional materials-based perovskite solar panels into a stand-alone solar farm, Nat. Energy 7 (2022) 597–607, https://doi.org/10.1038/s41560-022-01035-4.

[43] E. Mazzotta, T. Di Giulio, V. Mastronardi, P.P. Pompa, M. Moglianetti, C. Malitesta, Bare platinum nanoparticles deposited on glassy carbon electrodes for electrocatalytic detection of hydrogen peroxide, ACS Appl. Nano Mater. 4 (2021) 7650–7662, https://doi.org/10.1021/acsanm.1c00754.

[44] M. Moglianetti, E. De Luca, D. Pedone, R. Marotta, T. Catelani, B. Sartori, H. Amenitsch, S.F. Retta, P.P. Pompa, Platinum nanozymes recover cellular ROS homeostasis in an oxidative stress-mediated disease model, Nanoscale 8 (2016) 3739–3752, https://doi.org/10.1039/C5NR08358C.

[45] M. Moglianetti, J. Solla-Gullón, P. Donati, D. Pedone, D. Debellis, T. Sibillano, R. Brescia, C. Giannini, V. Montiel, J.M. Feliu, P.P. Pompa, Citrate-coated, size-tunable octahedral platinum nanocrystals: a novel route for advanced electrocatalysts, ACS Appl. Mater. Interfaces 10 (2018) 41608–41617, https://doi.org/10.1021/acsami.8b11774.

[46] V. Mastronardi, E. Magliocca, J.S. Gullon, R. Brescia, P.P. Pompa, T.S. Miller, M. Moglianetti, Ultrasmall, coating-free, pyramidal platinum nanoparticles for high stability fuel cell oxygen reduction, ACS Appl. Mater. Interfaces 14 (2022) 36570–36581, https://doi.org/10.1021/acsami.2c07738.

[47] P. Mariani, L. Najafi, G. Bianca, M.I. Zappia, L. Gabatel, A. Agresti, S. Pescetelli, A. Di Carlo, S. Bellani, F. Bonaccorso, Low-temperature graphene-based paste for large-area carbon perovskite solar cells, ACS Appl. Mater. Interfaces 13 (2021) 22368–22380, https://doi.org/10.1021/acsami.1c02626.

[48] S. Niu, S. Li, Y. Du, X. Han, P. Xu, How to reliably report the overpotential of an electrocatalyst, ACS Energy Lett. 5 (2020) 1083–1087, https://doi.org/10.1021/acsenergylett.0c00321.

[49] S. Anantharaj, S.R. Ede, K. Karthick, S. Sam Sankar, K. Sangeetha, P.E. Karthik, S. Kundu, Precision and correctness in the evaluation of electrocatalytic water splitting: revisiting activity parameters with a critical assessment, Energy Environ. Sci. 11 (2018) 744–771, https://doi.org/10.1039/C7EE03457A.

[50] S. Trasatti, O.A. Petrii, Real surface area measurements in electrochemistry, J. Electroanal. Chem. 327 (1992) 353–376, https://doi.org/10.1016/0022-0728(92)80162-W.

[51] K. Ehelebe, N. Schmitt, G. Sievers, A.W. Jensen, A. Hrnjić, P. Collantes Jiménez, P. Kaiser, M. Geuß, Y.P. Ku, P. Jovanovič, K.J.J. Mayrhofer, B. Etzold, N. Hodnik, M. Escudero-Escribano, M. Arenz, S. Cherevko, Benchmarking fuel cell electrocatalysts using gas diffusion electrodes: inter-lab comparison and best practices, ACS Energy Lett. 7 (2022) 816–826, https://doi.org/10.1021/acsenergylett.1c02659.

[52] P. Trinke, P. Haug, J. Brauns, B. Bensmann, R. Hanke-Rauschenbach, T. Turek, Hydrogen crossover in PEM and alkaline water electrolysis: mechanisms, direct comparison and mitigation strategies, J. Electrochem. Soc. 165 (2018) F502–F513, https://doi.org/10.1149/2.0541807jes.

[53] A. Morozan, H. Johnson, C. Roiron, G. Genay, D. Aldakov, A. Ghedjatti, C. T. Nguyen, P.D. Tran, S. Kinge, V. Artero, Nonprecious bimetallic iron−molybdenum sulfide electrocatalysts for the hydrogen evolution reaction in proton exchange membrane electrolyzers, ACS Catal. 10 (2020) 14336–14348, https://doi.org/10.1021/acscatal.0c03692.

[54] C. Lamy, P. Millet, A critical review on the definitions used to calculate the energy efficiency coefficients of water electrolysis cells working under near ambient temperature conditions, J. Power Sources 447 (2020), 227350, https://doi.org/10.1016/j.jpowsour.2019.227350.

[55] E. Auer, A. Freund, J. Pietsch, T. Tacke, Carbons as supports for industrial precious metal catalysts, Appl. Catal. A Gen. 173 (1998) 259–271, https://doi.org/10.1016/S0926-860X(98)00184-7.

[56] S. Pérez-Rodríguez, E. Pastor, M.J. Lázaro, Electrochemical behavior of the carbon black Vulcan XC-72R: influence of the surface chemistry, Int. J. Hydrog. Energy 43 (2018) 7911–7922, https://doi.org/10.1016/j.ijhydene.2018.03.040.

[57] A. Zanetta, I. Bulfaro, F. Faini, M. Manzi, G. Pica, M. De Bastiani, S. Bellani, M. I. Zappia, G. Bianca, L. Gabatel, J.K. Panda, A.E. Del Rio Castillo, M. Prato, S. Lauciello, F. Bonaccorso, G. Grancini, Enhancing charge extraction in inverted perovskite solar cells contacts via ultrathin graphene:fullerene composite interlayers, J. Mater. Chem. A (2023), https://doi.org/10.1039/D2TA07512A.

[58] J.B. Wu, M.L. Lin, X. Cong, H.N. Liu, P.H. Tan, Raman spectroscopy of graphene-based materials and its applications in related devices, Chem. Soc. Rev. 47 (2018) 1822–1873, https://doi.org/10.1039/C6CS00915H.

[59] A.C. Ferrari, D.M. Basko, Raman spectroscopy as a versatile tool for studying the properties of graphene, Nat. Nanotechnol. 8 (2013) 235–246, https://doi.org/10.1038/nnano.2013.46.

[60] M.A. Garakani, S. Bellani, V. Pellegrini, R. Oropesa-Nuñez, A.E.D.R. Castillo, S. Abouali, L. Najafi, B. Martín-García, A. Ansaldo, P. Bondavalli, C. Demirci, V. Romano, E. Mantero, L. Marasco, M. Prato, G. Bracciale, F. Bonaccorso, Scalable spray-coated graphene-based electrodes for high-power electrochemical double-layer capacitors operating over a wide range of temperature, Energy Storage Mater. 34 (2021) 1–11, https://doi.org/10.1016/j.ensm.2020.08.036.

[61] L. Najafi, R. Oropesa-Nuñez, B. Martín-García, F. Drago, M. Prato, V. Pellegrini, F. Bonaccorso, S. Bellani, Water-dispersible few-layer graphene flakes for selective and rapid ion mercury (Hg^{2+})-rejecting membranes, Mater. Adv. 1 (2020) 387–402, https://doi.org/10.1039/d0ma00060d.

[62] L. Najafi, S. Bellani, R. Oropesa-Nuñez, B. Martín-García, M. Prato, F. Bonaccorso, Single-/few-layer graphene as long-lasting electrocatalyst for hydrogen evolution

reaction, ACS Appl. Energy Mater. (2019), https://doi.org/10.1021/acsaem.9b00949.
[63] A. Eckmann, A. Felten, A. Mishchenko, L. Britnell, R. Krupke, K.S. Novoselov, C. Casiraghi, Probing the nature of defects in graphene by Raman spectroscopy, Nano Lett. 12 (2012) 3925–3930, https://doi.org/10.1021/nl300901a.
[64] H. Al-Johani, E. Abou-Hamad, A. Jedidi, C.M. Widdifield, J. Viger-Gravel, S. S. Sangaru, D. Gajan, D.H. Anjum, S. Ould-Chikh, M.N. Hedhili, A. Gurinov, M. J. Kelly, M. El Eter, L. Cavallo, L. Emsley, J.M. Basset, The structure and binding mode of citrate in the stabilization of gold nanoparticles, Nat. Chem. 9 (2017) 890–895, https://doi.org/10.1038/nchem.2752.
[65] M.A. Montiel, F.J. Vidal-Iglesias, V. Montiel, J. Solla-Gullón, Electrocatalysis on shape-controlled metal nanoparticles: progress in surface cleaning methodologies, Curr. Opin. Electrochem. 1 (2017) 34–39, https://doi.org/10.1016/j.coelec.2016.12.007.
[66] J.W. Park, J.S. Shumaker-Parry, Structural study of citrate layers on gold nanoparticles: role of intermolecular interactions in stabilizing nanoparticles, J. Am. Chem. Soc. 136 (2014) 1907–1921, https://doi.org/10.1021/ja4097384.
[67] M. Bajaj, N. Wangoo, D.V.S. Jain, R.K. Sharma, Quantification of adsorbed and dangling citrate ions on gold nanoparticle surface using thermogravimetric analysis, Sci. Rep. 10 (2020) 8213, https://doi.org/10.1038/s41598-020-65013-0.
[68] G.R. Bell, P.M. Dawson, P.A. Pandey, N.R. Wilson, P.A. Mulheran, Size-dependent mobility of gold nano-clusters during growth on chemically modified graphene, APL Mater. 2 (2014) 12109, https://doi.org/10.1063/1.4862696.
[69] W.J. Lee, S. Bera, C.M. Kim, E.K. Koh, W.P. Hong, S.J. Oh, E. Cho, S.H. Kwon, Synthesis of highly dispersed Pt nanoparticles into carbon supports by fluidized bed reactor atomic layer deposition to boost PEMFC performance, NPG Asia Mater. 12 (2020) 40, https://doi.org/10.1038/s41427-020-0223-x.
[70] C.A. Campos-Roldán, G. Ramos-Sánchez, R.G. Gonzalez-Huerta, J.R. Vargas García, P.B. Balbuena, N. Alonso-Vante, Influence of sp^3-sp^2 carbon nanodomains on metal/support interaction, catalyst durability, and catalytic activity for the oxygen reduction reaction, ACS Appl. Mater. Interfaces 8 (2016) 23260–23269, https://doi.org/10.1021/acsami.6b06886.
[71] N. Dubouis, A. Grimaud, The hydrogen evolution reaction: from material to interfacial descriptors, Chem. Sci. 10 (2019) 9165–9181, https://doi.org/10.1039/C9SC03831K.
[72] F.G. Will, Hydrogen adsorption on platinum single crystal electrodes, J. Electrochem. Soc. 112 (1965) 451, https://doi.org/10.1149/1.2423567.
[73] X. Chen, I.T. McCrum, K.A. Schwarz, M.J. Janik, M.T.M. Koper, Co-adsorption of cations as the cause of the apparent pH dependence of hydrogen adsorption on a stepped platinum single-crystal electrode, Angew. Chem. Int. Ed. 56 (2017) 15025–15029, https://doi.org/10.1002/anie.201709455.
[74] J. Clavilier, R. Faure, G. Guinet, R. Durand, Preparation of monocrystalline Pt microelectrodes and electrochemical study of the plane surfaces cut in the direction of the {111} and {110} planes, J. Electroanal. Chem. Interfacial Electrochem. 107 (1980) 205–209, https://doi.org/10.1016/S0022-0728(79)80022-4.
[75] M.J.T.C. van der Niet, N. Garcia-Araez, J. Hernández, J.M. Feliu, M.T.M. Koper, Water dissociation on well-defined platinum surfaces: the electrochemical perspective, Catal. Today 202 (2013) 105–113, https://doi.org/10.1016/j.cattod.2012.04.059.
[76] Z. Jie, S. Wenchao, Z. Zhongbin, X. Bingjun, Y. Yushan, Universal dependence of hydrogen oxidation and evolution reaction activity of platinum-group metals on pH and hydrogen binding energy, Sci. Adv. 2 (2022), e1501602, https://doi.org/10.1126/sciadv.1501602.
[77] X. Yang, J. Nash, N. Oliveira, Y. Yan, B. Xu, Understanding the pH dependence of underpotential deposited hydrogen on platinum, Angew. Chem. Int. Ed. 58 (2019) 17718–17723, https://doi.org/10.1002/anie.201909697.
[78] M. Bernt, H.A. Gasteiger, Influence of ionomer content in IrO_2/TiO_2 electrodes on PEM water electrolyzer performance, J. Electrochem. Soc. 163 (2016) F3179–F3189, https://doi.org/10.1149/2.0231611jes.
[79] K.A. Lewinski, D. van der Vliet, S.M. Luopa, NSTF advances for PEM electrolysis - the effect of alloying on activity of NSTF electrolyzer catalysts and performance of NSTF based PEM electrolyzers, ECS Trans. 69 (2015) 893–917, https://doi.org/10.1149/06917.0893ecst.
[80] M. Bühler, P. Holzapfel, D. McLaughlin, S. Thiele, From catalyst coated membranes to porous transport electrode based configurations in PEM water electrolyzers, J. Electrochem. Soc. 166 (2019) F1070–F1078, https://doi.org/10.1149/2.0581914jes.
[81] L. Najafi, S. Bellani, A. Castelli, M.P. Arciniegas, R. Brescia, R. Oropesa-Nuñez, B. Martín-García, M. Serri, F. Drago, L. Manna, F. Bonaccorso, Octapod-shaped CdSe nanocrystals hosting Pt with high mass activity for the hydrogen evolution reaction, Chem. Mater. 32 (2020) 2420–2429, https://doi.org/10.1021/acs.chemmater.9b04883.
[82] C. Wei, R.R. Rao, J. Peng, B. Huang, I.E.L. Stephens, M. Risch, Z.J. Xu, Y. Shao-Horn, Recommended practices and benchmark activity for hydrogen and oxygen electrocatalysis in water splitting and fuel cells, Adv. Mater. 31 (2019), 1806296, https://doi.org/10.1002/adma.201806296.
[83] S. Anantharaj, S. Noda, M. Driess, P.W. Menezes, The pitfalls of using potentiodynamic polarization curves for tafel analysis in electrocatalytic water splitting, ACS Energy Lett. 6 (2021) 1607–1611, https://doi.org/10.1021/acsenergylett.1c00608.
[84] D. Voiry, M. Chhowalla, Y. Gogotsi, N.A. Kotov, Y. Li, R.M. Penner, R.E. Schaak, P.S. Weiss, Best Practices for reporting electrocatalytic performance of nanomaterials, ACS Nano 12 (2018) 9635–9638, https://doi.org/10.1021/acsnano.8b07700.
[85] S. Anantharaj, S. Kundu, S. Noda, Worrisome exaggeration of activity of electrocatalysts destined for steady-state water electrolysis by polarization curves from transient techniques, J. Electrochem. Soc. 169 (2022) 14508, https://doi.org/10.1149/1945-7111/ac47ec.
[86] A.M. Harzandi, S. Shadman, M. Ha, C.W. Myung, D.Y. Kim, H.J. Park, S. Sultan, W.S. Noh, W. Lee, P. Thangavel, W.J. Byun, S. Lee, J.N. Tiwari, T.J. Shin, J. H. Park, Z. Lee, J.S. Lee, K.S. Kim, Immiscible bi-metal single-atoms driven synthesis of electrocatalysts having superb mass-activity and durability, Appl. Catal. B Environ. 270 (2020), 118896, https://doi.org/10.1016/j.apcatb.2020.118896.
[87] E. Hornberger, V. Mastronardi, R. Brescia, P.P. Pompa, M. Klingenhof, F. Dionigi, M. Moglianetti, P. Strasser, Seed-mediated synthesis and catalytic ORR reactivity of facet-stable, monodisperse platinum nano-octahedra, ACS Appl. Energy Mater. 4 (2021) 9542–9552, https://doi.org/10.1021/acsaem.1c01696.
[88] N. Cheng, S. Stambula, D. Wang, M.N. Banis, J. Liu, A. Riese, B. Xiao, R. Li, T. K. Sham, L.M. Liu, G.A. Botton, X. Sun, Platinum single-atom and cluster catalysis of the hydrogen evolution reaction, Nat. Commun. 7 (2016) 13638, https://doi.org/10.1038/ncomms13638.
[89] W. Ju, M.V.F. Heinz, L. Pusterla, M. Hofer, B. Fumey, R. Castiglioni, M. Pagani, C. Battaglia, U.F. Vogt, Lab-scale alkaline water electrolyzer for bridging material fundamentals with realistic operation, ACS Sustain. Chem. Eng. 6 (2018) 4829–4837, https://doi.org/10.1021/acssuschemeng.7b04173.
[90] K. Ehelebe, D. Seeberger, M.T.Y. Paul, S. Thiele, K.J.J. Mayrhofer, S. Cherevko, Evaluating electrocatalysts at relevant currents in a half-cell: the impact of Pt loading on oxygen reduction reaction, J. Electrochem. Soc. 166 (2019) F1259–F1268, https://doi.org/10.1149/2.0911915jes.
[91] G. Bender, M. Carmo, T. Smolinka, A. Gago, N. Danilovic, M. Mueller, F. Ganci, A. Fallisch, P. Lettenmeier, K.A. Friedrich, K. Ayers, B. Pivovar, J. Mergel, D. Stolten, Initial approaches in benchmarking and round robin testing for proton exchange membrane water electrolyzers, Int. J. Hydrog. Energy 44 (2019) 9174–9187, https://doi.org/10.1016/j.ijhydene.2019.02.074.
[92] H. Chen, J. Li, Y. Shen, W. Jiao, J. Wang, Y. Zou, X. Zou, Room temperature, fast fabrication of square meter-sized oxygen evolution electrode toward industrial alkaline electrolyzer, Appl. Catal. B Environ. 316 (2022), 121605, https://doi.org/10.1016/j.apcatb.2022.121605.
[93] B. Zayat, D. Mitra, S.R. Narayanan, Inexpensive and efficient alkaline water electrolyzer with robust steel-based electrodes, J. Electrochem. Soc. 167 (2020), 114513, https://doi.org/10.1149/1945-7111/aba792.
[94] H. Schäfer, K. Küpper, M. Schmidt, K. Müller-Buschbaum, J. Stangl, D. Daum, M. Steinhart, C. Schulz-Kölbel, W. Han, J. Wollschläger, U. Krupp, P. Hou, X. Liu, Steel-based electrocatalysts for efficient and durable oxygen evolution in acidic media, Catal. Sci. Technol. 8 (2018) 2104–2116, https://doi.org/10.1039/C7CY02194A.
[95] A. Abdel Haleem, J. Huyan, K. Nagasawa, Y. Kuroda, Y. Nishiki, A. Kato, T. Nakai, T. Araki, S. Mitsushima, Effects of operation and shutdown parameters and electrode materials on the reverse current phenomenon in alkaline water analyzers, J. Power Sources 535 (2022), 231454, https://doi.org/10.1016/j.jpowsour.2022.231454.
[96] C. Schnuelle, T. Wassermann, D. Fuhrlaender, E. Zondervan, Dynamic hydrogen production from PV & wind direct electricity supply - modeling and techno-economic assessment, Int. J. Hydrog. Energy 45 (2020) 29938–29952, https://doi.org/10.1016/j.ijhydene.2020.08.044.
[97] N. Todoroki, T. Wadayama, Electrochemical stability of stainless-steel-made anode for alkaline water electrolysis: surface catalyst nanostructures and oxygen evolution overpotentials under applying potential cycle loading, Electrochem. Commun. 122 (2021), 106902, https://doi.org/10.1016/j.elecom.2020.106902.
[98] Y. Uchino, T. Kobayashi, S. Hasegawa, I. Nagashima, Y. Sunada, A. Manabe, Y. Nishiki, S. Mitsushima, Relationship between the redox reactions on a bipolar plate and reverse current after alkaline water electrolysis, Electrocatalysis 9 (2018) 67–74, https://doi.org/10.1007/s12678-017-0423-5.
[99] J. Brauns, J. Schönebeck, M.R. Kraglund, D. Aili, J. Hnát, J. Žitka, W. Mues, J. O. Jensen, K. Bouzek, T. Turek, Evaluation of diaphragms and membranes as separators for alkaline water electrolysis, J. Electrochem. Soc. 168 (2021) 14510, https://doi.org/10.1149/1945-7111/abda57.
[100] Energy, Hydrogen Production: Electrolysis, U. S. Department of Energy, 2022. https://www.energy.gov/eere/fuelcells/hydrogen-production-electrolysis.